

## SUPPORTING INFORMATION

# Nanoporous $\text{YVO}_4$ as a Luminescent Host for Probing Molecular Encapsulation

Milena Lima Brito,<sup>a</sup> Steven Huband,<sup>b</sup> Marc Walker,<sup>b</sup> Richard I. Walton,<sup>c</sup> and  
Paulo C. de Sousa Filho<sup>\*a</sup>

<sup>a</sup>Department of Inorganic Chemistry, Institute of Chemistry, University of Campinas (Unicamp),  
R. Monteiro Lobato, 270, 13083-970, Campinas, São Paulo, Brazil

<sup>b</sup>Department of Physics, University of Warwick, Coventry, CV4 7AL, United Kingdom.

<sup>c</sup>Department of Chemistry, University of Warwick, Coventry, CV4 7AL, United Kingdom.

\*Corresponding author: pcsfilho@unicamp.br

# TOC

	Page
<b>1. EXPERIMENTAL DETAILS .....</b>	<b>S1</b>
<b>1.1. Starting materials and precursors .....</b>	<b>S1</b>
<b>1.2. Reverse microemulsions .....</b>	<b>S2</b>
<b>1.3. Nanoparticle synthesis and dye encapsulation .....</b>	<b>S4</b>
<b>1.4. Characterisation .....</b>	<b>S6</b>
<b>2. ADDITIONAL FIGURES AND PROCESSING DETAILS .....</b>	<b>S8</b>
<b>2.1. Water-in-<i>n</i>-dodecane reverse microemulsions .....</b>	<b>S8</b>
<b>2.2. Characterisation of REVO<sub>4</sub> nanoparticles .....</b>	<b>S13</b>
<b>2.3. Luminescence characterisation .....</b>	<b>S18</b>
<b>2.4. Upconversion luminescence .....</b>	<b>S21</b>
<b>2.5. Dye encapsulation in (Y,Eu)VO<sub>4</sub> particles .....</b>	<b>S23</b>
<b>3. REFERENCES .....</b>	<b>S26</b>

## 1. EXPERIMENTAL DETAILS

### 1.1. Starting materials and precursors

Sodium orthovanadate ( $\text{Na}_3\text{VO}_4$  – 99.98%; Sigma-Aldrich), sodium metavanadate ( $\text{NaVO}_3$  – 98%; Sigma-Aldrich), rare earth oxides ( $\text{Y}_2\text{O}_3$ ,  $\text{Yb}_2\text{O}_3$ , and  $\text{Eu}_2\text{O}_3$  – 99.99%; Sigma-Aldrich), erbium(III) nitrate pentahydrate ( $\text{Er}(\text{NO}_3)_3 \cdot 5\text{H}_2\text{O}$  – 99.99%; Sigma-Aldrich), sodium hydroxide (97%; Synth), hydrochloric acid (37% w/w; Synth), ethanol (98%; Vetec), oleic acid (oleH, 90%; Sigma-Aldrich), hexadecyltrimethylammonium bromide (CTAB, 99%; Sigma-Aldrich), 1-hexanol (98%; Sigma-Aldrich), *n*-dodecane (99.9%; Sigma-Aldrich), xylenol orange (XO, 99%; Sigma-Aldrich), methylene blue (MB, 99%; Sigma-Aldrich), and rose Bengal (RB, 99%; Sigma-Aldrich) were used without further purification. Aqueous RE chloride solutions ( $0.2 \text{ mol L}^{-1}$ ) were prepared by dissolution of previously calcined RE oxides ( $900 \text{ }^\circ\text{C}$ , 30 min) in concentrated HCl at  $70 \text{ }^\circ\text{C}$  followed by adjustment of the pH to 5.8-6.2 via evaporation. The RE oleate complexes ( $[\text{RE}(\text{ole})_3(\text{H}_2\text{O})_2]$ ) used as sources of  $\text{RE}^{3+}$  in the synthesis of the nanoparticles were prepared following literature adaptations.<sup>1</sup> Firstly, 6 mmol of NaOH were dissolved in 10 mL of ethanol at  $25 \text{ }^\circ\text{C}$ . Then, a solution containing 6 mmol of oleic acid in ethanol ( $0.6 \text{ mol L}^{-1}$ ) was added, and the mixture was kept under stirring for 20 min. A 9:1 (v/v) mixture of aqueous  $\text{YCl}_3$  ( $0.2 \text{ mol L}^{-1}$ ) and  $\text{EuCl}_3$  ( $0.2 \text{ mol L}^{-1}$ ) solutions was added to obtain a white suspension. The mixture was stirred for 7 h at  $25 \text{ }^\circ\text{C}$  and stored at  $5 \text{ }^\circ\text{C}$  for 12 h. The solid product composed by yttrium and europium oleates (*i.e.*,  $[(\text{Y},\text{Eu})(\text{ole})_3(\text{H}_2\text{O})_2]$ , 90%  $\text{Y}^{3+}$ , 10%  $\text{Eu}^{3+}$  mol/mol) was recovered and purified by centrifugation and resuspension in water:ethanol 1:1 v/v ( $\sim 300 \text{ mL}$ ), and dried at reduced pressure (Figure S1). The oleate precursors containing  $\text{Y}^{3+}$ ,  $\text{Yb}^{3+}$ , and  $\text{Er}^{3+}$  (*i.e.*,  $[(\text{Y},\text{Yb},\text{Er})(\text{ole})_3(\text{H}_2\text{O})_2]$ , 78%  $\text{Y}^{3+}$ , 20%  $\text{Yb}^{3+}$  and 2%  $\text{Er}^{3+}$  mol/mol) were prepared by the

same protocol, using a 7.8:2.0:0.2 (v/v) mixture of aqueous  $\text{YCl}_3$  (0.2 mol  $\text{L}^{-1}$ ),  $\text{YbCl}_3$  (0.2 mol  $\text{L}^{-1}$ ) and  $\text{Er}(\text{NO}_3)_3$  (0.2 mol  $\text{L}^{-1}$ ) solutions.

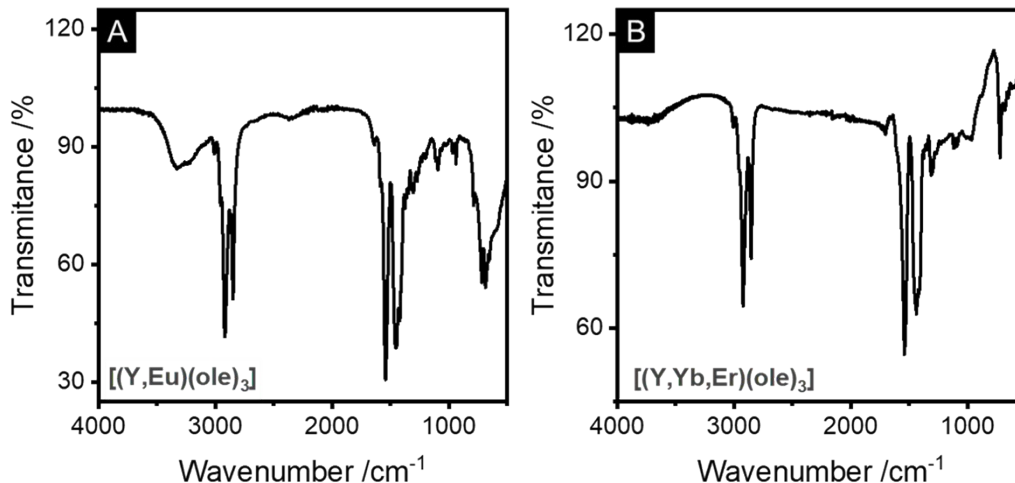


**Figure S1.** Fourier transform infrared (FTIR) spectra of the rare earth oleates used as precursors: (A)  $[(\text{Y},\text{Eu})(\text{ole})_3(\text{H}_2\text{O})_2]$ . (B)  $[(\text{Y},\text{Yb},\text{Er})(\text{ole})_3(\text{H}_2\text{O})_2]$ .

## 1.2. Reverse microemulsions

Water-in-*n*-dodecane reverse microemulsions were used as soft templates for the crystallisation of RE vanadates. The water:*n*-dodecane volume ratio was set as 1:25 (v/v) in all cases, and the aqueous phases consisted in 0.05 mol  $\text{L}^{-1}$   $\text{Na}_3\text{VO}_4$  or  $\text{NaVO}_3$  solutions. The effect of the pH of the aqueous phases and of the nature of the vanadium precursor were investigated as described further. A 44% w/w mixture of CTAB in 1-hexanol with 0.917 g  $\text{cm}^{-3}$  density was used as the surfactant/cosurfactant system. The composition of the microemulsions was optimised with respect to the water/CTAB molar ratio (herein denoted  $W_0$ ). For this, biphasic systems containing 0.2 mL of aqueous 0.05 mol  $\text{L}^{-1}$   $\text{Na}_3\text{VO}_4$  and 5 mL of *n*-dodecane were prepared. Then, 50  $\mu\text{L}$  aliquots of the CTAB/1-hexanol 44% (w/w) mixture were added under stirring until single microemulsion phases were formed, which was verified by the absence of turbidity. The

minimum amount of CTAB/1-hexanol necessary for the formation of a single phase was 500  $\mu\text{L}$ , and addition of more than 5 mL of the CTAB/1-hexanol mixture broke the microemulsions. Therefore, microemulsions with  $W_{\text{O}}$  molar ratios of 30, 25, 20, 15, 12, 10 were characterised by dynamic light scattering and small angle X-ray scattering to determine the optimum  $W_{\text{O}}$  ratio with respect to mean hydrodynamic diameters ( $d_{\text{H}}$ ), polydispersity (PDI), and amount of required surfactant (Figure S2). Based on these aspects, we chose microemulsions with  $W_{\text{O}}=25$  to test the crystallization of the  $\text{REVO}_4$  nanoparticles.

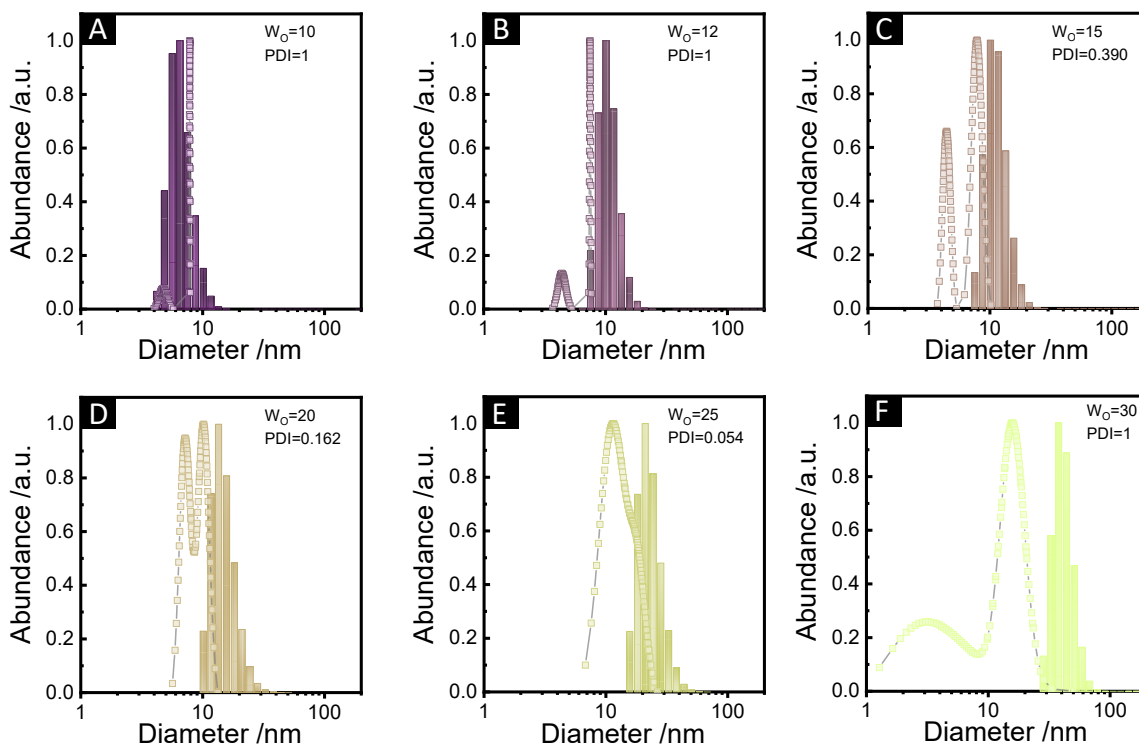


**Figure S2.** Size distributions in number obtained by dynamic light scattering (bars) and small-angle X-ray scattering (points) for the different water-in-*n*-dodecane microemulsions with (A)  $W_{\text{O}}=10$ , (B)  $W_{\text{O}}=12$ , (C)  $W_{\text{O}}=15$ , (D)  $W_{\text{O}}=20$ , (E)  $W_{\text{O}}=25$ , and (F)  $W_{\text{O}}=30$ . The scales on the vertical axes correspond to arbitrary abundances normalised to 1. (PDI=polydispersity index).

### 1.3. Nanoparticle synthesis and dye encapsulation

In a typical procedure with  $W_O=25$ , 27 mL of *n*-dodecane and 1.08 mL of aqueous 0.05 mol L<sup>-1</sup> Na<sub>3</sub>VO<sub>4</sub> were stirred for 30 min in a 50 mL flask. The pH of the aqueous phase was previously adjusted to 11.5 with 0.01 mol L<sup>-1</sup> HCl(aq.). Then, 2.51 mL of the CTAB/1-hexanol mixture (44% w/w) were added to form a clear microemulsion, which was homogenised under stirring for 24 h at 25 °C. Finally, 2 mL of the initial microemulsion was removed for further DLS characterisation, and 5 mL of a 0.01 mol L<sup>-1</sup> solution of the [(Y,Eu)(ole)<sub>3</sub>(H<sub>2</sub>O)<sub>2</sub>] complex in *n*-dodecane were dropped (300 μL min<sup>-1</sup>) under stirring. The lipid microemulsion containing RE<sup>3+</sup> and vanadate precursors was kept at 25 °C under stirring for 14 h, becoming turbid at the end. The final (Y,Eu)VO<sub>4</sub> particles were recovered by centrifugation (2x10<sup>4</sup>g) and washed with ethanol (80 mL) and water (80 mL) before drying at 12 h in a under reduced pressure in a desiccator over silica. The preparation of (Y,Yb,Er)VO<sub>4</sub> particles involved the same procedure using the [(Y,Yb,Er)(ole)<sub>3</sub>(H<sub>2</sub>O)<sub>2</sub>] complex instead of the Y/Eu precursor. In addition, the effect of the pH of aqueous phase on the formation of the particles was evaluated by replacing the pH=11.5 aqueous solution by 0.05 mol L<sup>-1</sup> solutions of Na<sub>3</sub>VO<sub>4</sub> (pH=13) or NaVO<sub>3</sub> (pH=7) in deionized water. We also tested the functionalization of the (Y,Eu)VO<sub>4</sub> nanoparticles with methylene blue (MB), xylene orange (XO), and rose Bengal (RB) dyes by two distinct protocols, namely encapsulation and adsorption. For the encapsulation test, the optimized synthesis protocol with  $W_O=25$  and pH=11.5 was applied, using aqueous phases containing 10<sup>-4</sup> mol L<sup>-1</sup> of the solubilized dyes. The purification of the particles followed the same procedure of washing with ethanol (80 mL) and water (80 mL). The adsorption of dyes in the external surface of the particles comprised the preparation of (Y,Eu)VO<sub>4</sub> by the optimised protocol ( $W_O=25$  and pH=11.5) followed by particle purification by centrifugation. In this case,

1.8 mL of  $10^{-4}$  mol L<sup>-1</sup> XO solution were added to the purified solid particles and the resulting suspension was left under stirring with a magnetic bar at  $\sim 25$  °C for 14 h. The solid product was recovered by centrifugation at ( $2 \times 10^4$  g) and purified again via centrifugation and washing with ethanol (20 mL) and water (20 mL). The functionalisation of the particles was evaluated in terms of xylene orange release in different pH conditions and different times by UV-Vis absorption spectroscopy. For this, 0.7 mg mL<sup>-1</sup> stock aqueous suspensions of (Y,Eu)VO<sub>4</sub> nanoparticles containing encapsulated xylene orange (*i.e.* XO@NP) or with modified external surface (*i.e.*, NP@XO) were prepared. Aliquots of 100  $\mu$ L of these suspensions were dispersed in 2 mL of NaOH or HCl aqueous solutions with pH between 3 and 12. The nanoparticles were left to stand at these pH conditions (3-12) for 30 days for comparison. After this period, the particles were centrifuged, and the supernatants were analysed by UV-Vis spectroscopy. Based on the results obtained from the described tests, the release of XO from XO@NP and NP@XO systems was evaluated by exposing the 4 mg of the particles to 2 mL of a pH=11 NaOH aqueous solution for 1 h at 50 °C in an ultrasonic bath. After centrifugation, the supernatants were analysed by UV-Vis spectroscopy to detect the XO absorption at 580 nm ( $\epsilon=3.12 \times 10^4$  L mol<sup>-1</sup> cm<sup>-1</sup>).<sup>2</sup> The centrifuged nanoparticles were resuspended in 2 mL of aqueous NaOH with pH 11 and kept again for 1 h at 50 °C. This procedure was repeated four times, totalizing 5 washing cycles to induce the release of XO molecules from the XO@NP and NP@XO systems.

#### 1.4. Characterisation

Fourier-transform infrared spectroscopy (FTIR) was performed via attenuated total reflection using an Agilent Cary 630 spectrometer with a diamond crystal. Raman spectra were collected in a Horiba Scientific T64000 spectrometer equipped with a 633 nm HeNe laser. Dynamic light scattering (DLS) profiles of  $\sim 1 \text{ mg mL}^{-1}$  suspensions were measured on a Malvern Zetasizer NanoZS equipment ( $\lambda=633 \text{ nm}$ ,  $4 \text{ mW}$ ,  $173^\circ$ ) to access hydrodynamic diameters and  $\zeta$  potentials.  $\zeta$  potential vs. pH curves were measured by dispersing the particles ( $\sim 1 \text{ mg mL}^{-1}$ ) in  $1 \text{ mmol L}^{-1}$  NaCl aqueous solutions with pH=4-12 adjusted by addition of HCl or NaOH. Powder X-ray diffraction (XRD) was performed in a Shimadzu XRD 7000 diffractometer using Cu  $K\alpha_{1+2}$  radiation ( $\lambda = 1.5418 \text{ \AA}$ ). Different steps ( $0.02^\circ$  or  $0.1^\circ$ ) and integration times ( $0.6 \text{ s}$  and  $10 \text{ s}$ ) were applied to afford suitable diffraction intensities depending on the sample. Small- (SAXS) and wide-angle (WAXS) X-ray scattering profiles were measured on a Xenocs Xeuss 2.0 beamline equipped with a Cu  $K\alpha$  source microfocus ( $\lambda = 1.54189 \text{ \AA}$ ) with a  $0.8 \text{ mm}$  diameter beam, and a Pilatus 300k detector (pixel  $0.172 \text{ mm} \times 0.172 \text{ mm}$ ). The samples were placed in  $1 \text{ mm}$  thick borosilicate glass capillaries as sample holders. The scattering profiles ( $\sim 0.04$  to  $1.6 \text{ nm}^{-1}$ ) were obtained by azimuthal integration of raw 2D scattering profiles correcting sample thickness, absorption, solvent background. The scattering profiles were modelled using the Irena package<sup>3</sup> considering core@shell-type spheres (*i.e.*, microemulsions) or multiple populations of spheroids (*i.e.* suspensions of final particles). Size distributions in Figure 1G-I of the main text considered 2-population log-normal distributions of spheroid discontinuities (*i.e.* particles and nanopores inside particles, both with aspect ratio=1) in a diluted system. The morphology of the particles was analysed by scanning electron microscopy (SEM) on a Quanta FEG 250 HV microscope (SE and BSE), and by transmission electron microscopy (TEM) on JEOL JEM2100

LaB<sub>6</sub>, JEM-2100F, and ARM 200F microscopes (200 kV). X-ray photoelectron spectroscopy (XPS) data were collected on a Kratos Axis Ultra spectrometer with an Al K $\alpha$  monochromatic X-ray source (1486.7 eV) and detection at 90° to the sample surface. The base pressure of the spectrometer was approximately  $5 \times 10^{-11}$  mbar. XPS peaks were fitted by Voigt curves (Gaussian+Lorentzian) and Shirley-type baselines using CasaXPS software, enabling quantitative compositional information by considering relative areas of the different components after peak deconvolution. Luminescence spectroscopy was conducted on a Horiba Fluorolog 3 (FL3-22-iHR320) spectrofluorometer, equipped with Hamamatsu R928P detector, and continuous Xe lamp (450 W) or laser (CrystaLaser, DL 980-1W0-TO 4901  $\lambda_{\text{exc}}=980$  nm) excitation sources. The UV-Vis absorption spectra were acquired on 1 cm quartz cells on an Agilent Cary 50 UV-Vis spectrophotometer.

## 2. ADDITIONAL FIGURES AND PROCESSING DETAILS

### 2.1. Water-in-*n*-dodecane reverse microemulsions

The SAXS profiles (Fig. S3A) of the microemulsions with  $W_O=10-30$  were fitted as Gaussian size distributions of core-shell-type spheres as a model for the reverse micelles, where the total radius of the droplets is given by a sum of the inner radius of the core (*i.e.*, confined aqueous phase) and the thickness of the shell (*i.e.*, surfactant chains). The scattering length density (SLD) of *n*-dodecane has been calculated ( $SLD=7.33 \times 10^{-6} \text{ \AA}^{-2}$ ) and then fixed during the modelling, and SLD for the modeled shell and core has been allowed to refine (Table S1). The increase in the scattering intensity at low scattering vectors ( $q=4\pi \sin\theta/\lambda$ , where  $2\theta$  corresponds to the scattering angle) in systems showing agglomeration of micellar structures (Fig. S3A,  $W_O=30$  and  $W_O=25$ ) was modelled using a decaying power law (Eq. S1):<sup>3,4</sup>

$I(q) = B e^{\left(-q^2 R_g^2/3\right)} q^{-P},$	(S1)
--	------

where  $R_g$  is the gyration radius of the core@shell sphere, B is a scale factor and P is related to the type of scattering from smooth surfaces to fractal materials.<sup>3,4</sup> The fits resulted in a nearly constant thickness of 1.6 nm (Table S1), which is consistent with the chain size of CTAB.<sup>5</sup> The inner diameters of the micellar structures increased from ~2 to ~9 nm (Fig. S3B) with higher  $W_O$  ratios, yielding SAXS-modelled total diameters ranging from ~5 to ~12 nm (Table S1).

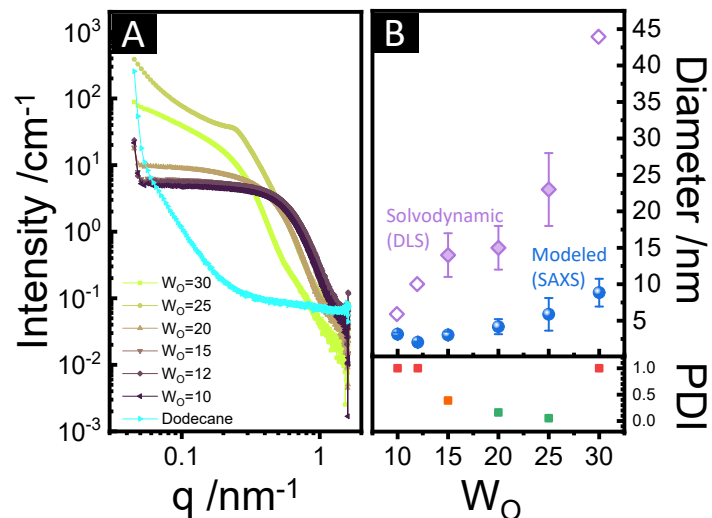


**Figure S3.** (A) SAXS profiles (scattered intensity vs. scattering vector,  $q$ ) of the water-in- $n$ -dodecane reverse microemulsions containing 0.05 mol L<sup>-1</sup> Na<sub>3</sub>VO<sub>4</sub> (pH=11.5) as aqueous phase using CTAB/1-hexanol as surfactant/cosurfactant in different H<sub>2</sub>O/CTAB molar ratios ( $W_o$ ). The scattering of pure  $n$ -dodecane was used as a reference for further modeling of the SAXS profiles. (B) (top) Mean diameters of micellar structures in the reverse microemulsions as a function of the  $W_o$  ratio: solvodynamic diameters calculated from DLS number distributions (magenta diamonds) and inner micellar diameters modelled from SAXS (blue spheres); the polydispersity indices (PDI) obtained from DLS distributions are shown at the bottom. Error bars were omitted for empty symbols in (B) due to the high PDI values.

**Table S1.** Inner micellar radii (core), thickness of the surfactant film (shell, Å) and difference between scattering length densities ( $\Delta\rho_{\text{core/shell}}$ ) modelled from SAXS measurements

$W_O$	Inner radius /Å	Thickness /Å	Total diameter /nm	$\Delta\rho_{\text{core/shell}} 10^{-6} / \text{Å}^{-2}$
30	44±19	17±1	12±3	0.189
25	29±22	16±1	9.1±2.4	0.005
20	21±10	16±2	7.4±1.2	0.102
15	15±4	16±6	6.2±1.0	0.313
12	10±1	16±7	5.3±0.8	0.284
10	16±4	17±5	6.5±0.7	0.134
25 (pH=7.0)	30±12	15±1	9.1±1.8	0.085
25 (pH=13)	28±11	16±1	8.9±1.7	0.138

Considering both size distributions and dynamic light scattering (DLS) polydispersity indices, the microemulsions with water/surfactant ratios ( $W_O$ )  $W_O = 20$  and  $W_O = 25$  induced the interface precipitation of the vanadate phase;  $W_O = 25$  was further investigated. The formation kinetics of  $\text{REVO}_4$  solids from aqueous precursors usually follows a non-classic nucleation/growth mechanism, being strongly dependent on the pH because of vanadate speciation and formation of non-crystalline metastable intermediates. Highly basic pH results in higher concentrations of  $\text{VO}_4^{3-}(\text{aq})$ , but also induces competitive precipitation of kinetically stable RE hydroxides. Conversely, acidic metavanadate ( $(\text{VO}_3)_n^{n-}$ ) solutions show a smaller availability of free  $\text{VO}_4^{3-}$  and may lead to the parallel precipitation of polyvanadates.

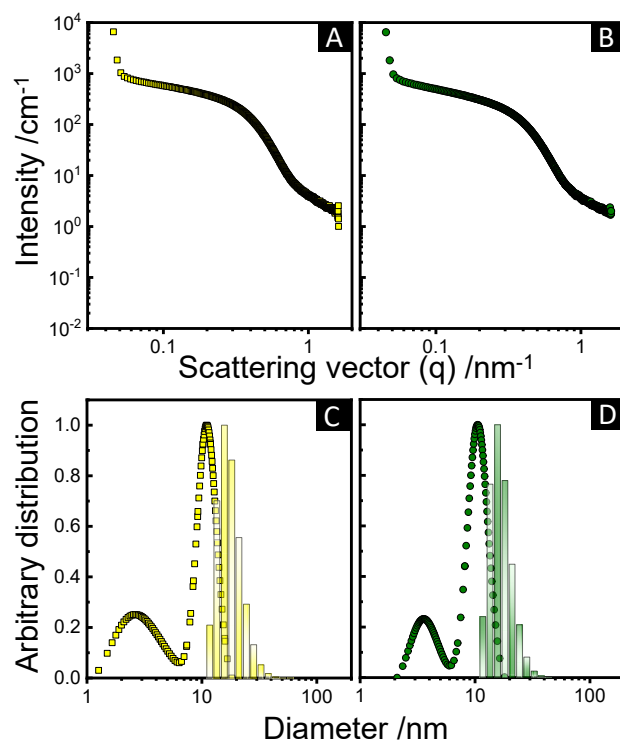


**Figure S4.** (A,B) SAXS profiles and (C,D) size distributions obtained water-in-*n*-dodecane microemulsions with  $W_o=25$  at different pHs of the aqueous phase, namely (A,C) pH=7.0 and (B,D) pH=13. Sizes in (C,D) correspond to number distributions obtained from fittings of SAXS curves (points) and dynamic light scattering (bars). (C) DLS:  $D_H=15\pm 4$  nm, PDI=0.2; (D) DLS:  $D_H=17\pm 4$  nm, PDI=0.3 ( $D_H$  corresponds to solvodynamic diameters obtained by fitting DLS profiles by lognormal distributions).

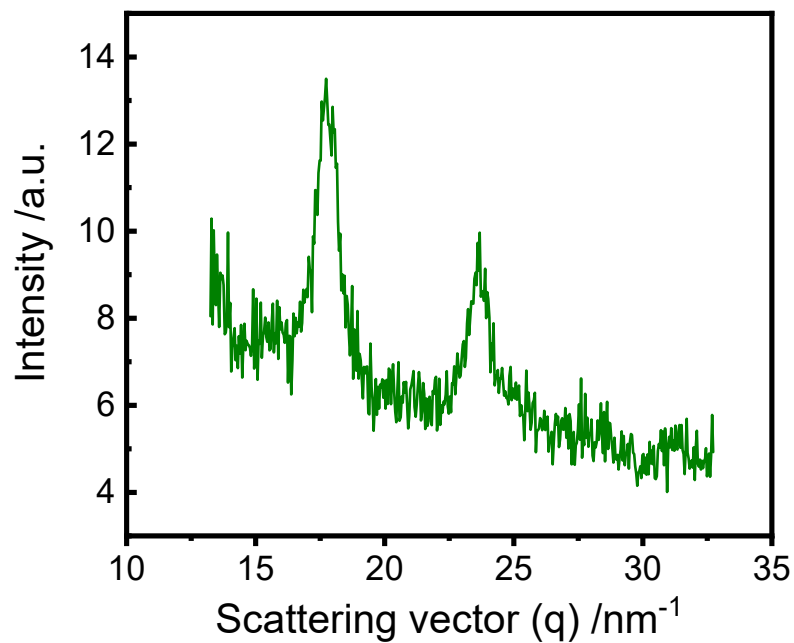


**Figure S5.** WAXS profile of the product obtained at ME system with pH 13.

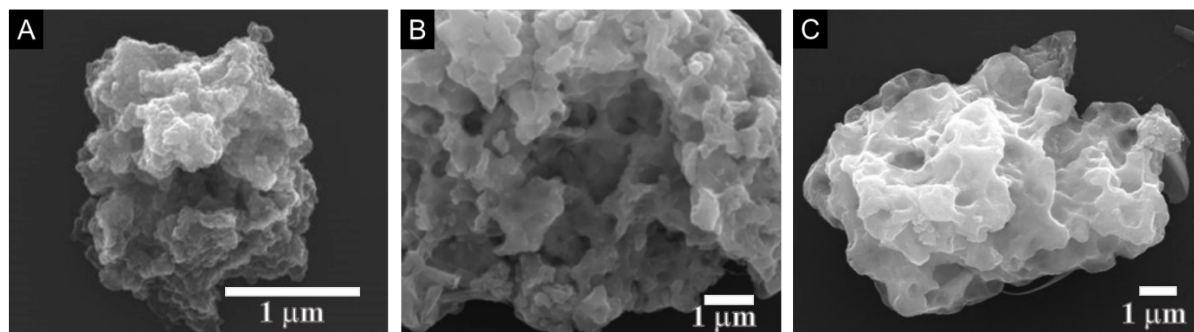


**Figure S6.** Scanning electron microscopy images of the (Y,Eu)VO<sub>4</sub> particles recovered from the reverse microemulsion synthesis performed with  $W_O=25$  and pH=7.

## 2.2. Characterisation of REVO<sub>4</sub> nanoparticles

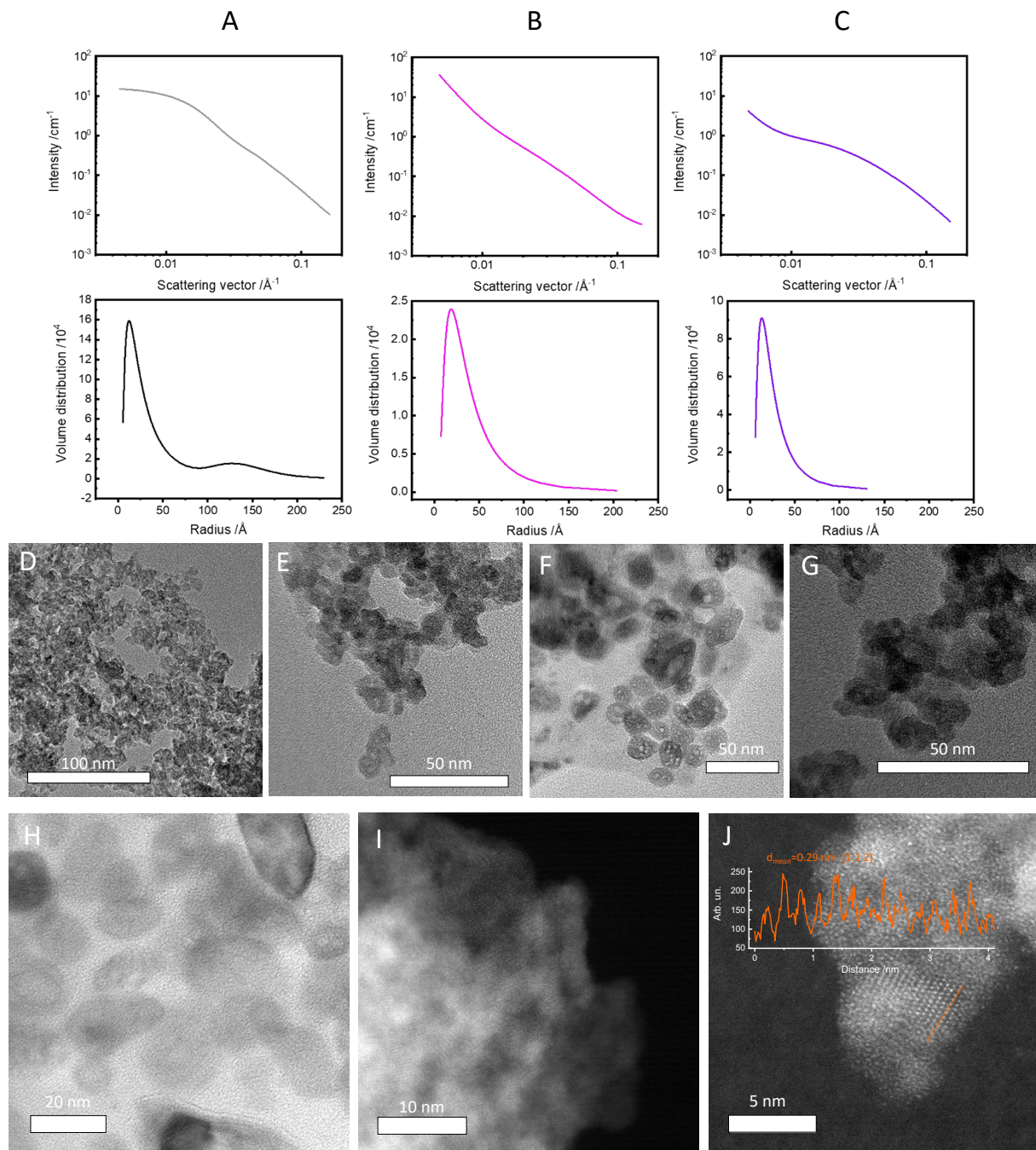


**Figure S7.** (A-C) Modelled SAXS profiles (above) and particle volume distributions (below) of (A) non-modified (Y,Eu)VO<sub>4</sub> nanoparticles, and particles synthesised at the same conditions containing encapsulated (B) rose Bengal (RB@NP, rose), or (C) xylenol orange (XO@NP, purple). (D-J) Transmission electron microscopy images (TEM and HRTEM) of (Y,Eu)VO<sub>4</sub> nanoparticles synthesised in reverse microemulsions ( $W_0=25$ , pH=11.5). The scattering profiles

at small angles in A-C were fitted by a model of spheroidal particles containing inner cavities and different degrees of interparticle aggregation. In this model, the electronic density discontinuities providing scattering at low angles mainly comprise the pores inside the particles, the inter-particle regions on aggregates, and the isolated particles in suspension. The scattering arising from the aggregate/solvent contrast is not observable in SAXS profiles because aggregate sizes may reach up to hundreds of nanometres. Size distributions obtained from SAXS refer mainly to the inner porosity of the particles (yielding pore sizes around 6-7 nm).

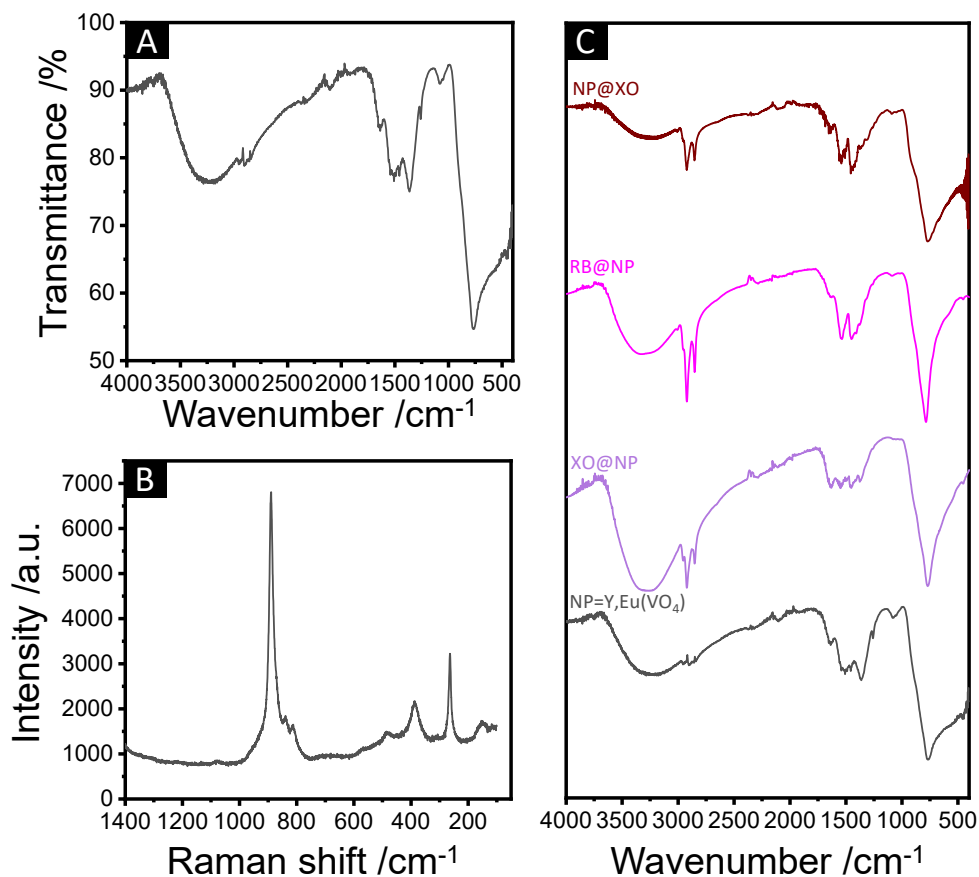


**Figure S8.** Infrared (A,C) and Raman (B) spectra of the vanadate nanoparticles synthesised via reverse microemulsion synthesis at the optimised conditions (pH=11.5 and  $W_0=25$ ). (A) FTIR and (B) Raman spectra of the non-functionalised (Y,Eu)VO<sub>4</sub> particles. (C) Comparison between infrared spectra of non-functionalized (Y,Eu)VO<sub>4</sub> particles (grey line, NP) and particles containing encapsulated XO (purple, XO@NP), encapsulated RB (rose, RB@NP), or adsorbed XO (wine, NP@XO). REVO<sub>4</sub> signals:  $\nu_1$ /V-O sym. stretch. (A<sub>1</sub>), 889 cm<sup>-1</sup>;  $\nu_3$ /V-O asym. stretch. (B<sub>2</sub>+E), 839, 812 cm<sup>-1</sup>;  $\nu_2$ /VO<sub>4</sub> sym. bend. (A<sub>1</sub>+B<sub>1</sub>), 388 cm<sup>-1</sup>;  $\nu_4$ /VO<sub>4</sub> asym. bend. (B<sub>2</sub>+E), 567, 491 cm<sup>-1</sup>. Signals of residual surfactants and solvents: [ $\nu_{OH}$ , 3713-2999 cm<sup>-1</sup> (water);  $\nu_{CH}$ , 2950-2825 cm<sup>-1</sup> (CTAB/1-hexanol, *n*-dodecane, oleate);  $\delta_{HOH}$ , 1639 cm<sup>-1</sup> (water);  $\nu_{COO^-}$ , 1508 cm<sup>-1</sup> (oleate);  $\delta_{CH_2}$ , 1258 cm<sup>-1</sup> (CTAB/1-hexanol, *n*-dodecane, oleate)].

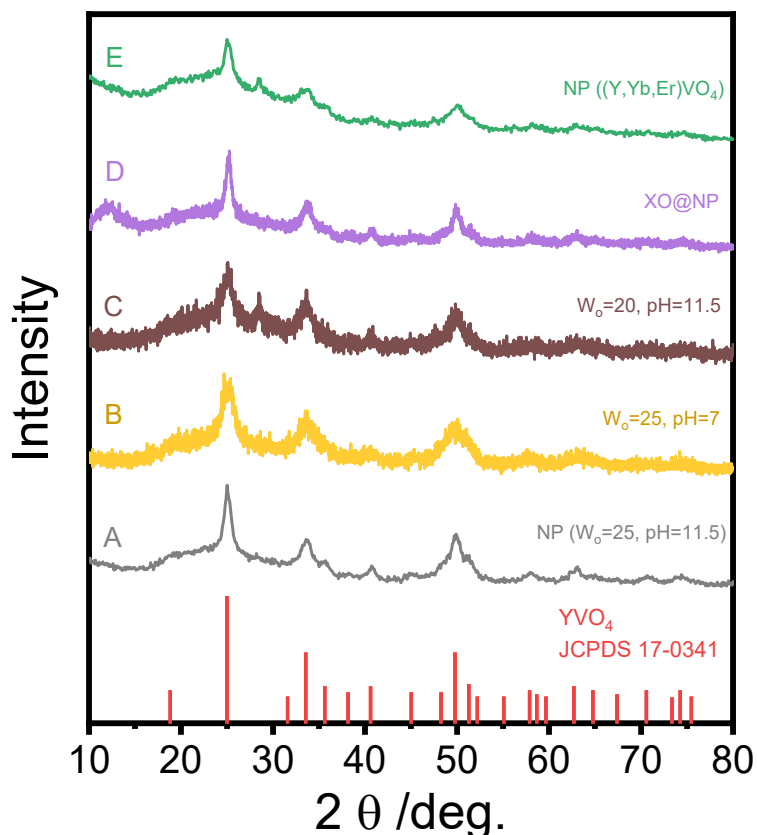


**Figure S9.** Powder X-ray diffraction profiles of (A-D) (Y,Eu)VO<sub>4</sub> and (E) (Y,Yb,Er)VO<sub>4</sub> nanoparticles obtained by reverse microemulsion synthesis at different conditions, namely (A) W<sub>0</sub>=25, pH=11.5 (*i.e.*, optimised conditions), (B) W<sub>0</sub>=25, pH=7; (C) W<sub>0</sub>=20, pH=11.5, (D) W<sub>0</sub>=25, pH=11.5 in the presence of XO (*i.e.*, XO@NP), and (E) W<sub>0</sub>=25, pH=11.5, with composition adapted for upconversion luminescence. The particles prepared in W<sub>0</sub>=25 and pH=13 could not be recovered from the reaction mixture as a powder (see Fig. S5 for WAXS). The crystalline coherence length estimated<sup>6</sup> for the (200) direction ranged between 7 and 9 nm for bare and XO- or RB-functionalized particles, suggesting no influence of the dye molecules on the crystalline growth.

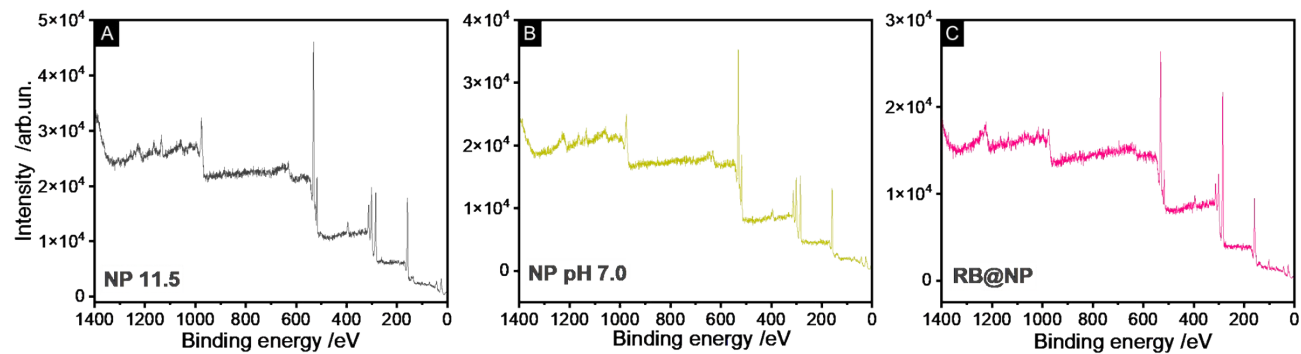


**Figure S10.** Survey XPS spectra of (Y,Eu)VO<sub>4</sub> nanoparticles obtained by reverse microemulsion synthesis at (A) W<sub>0</sub>=25, pH=11.5 and (B) W<sub>0</sub>=25 pH 7.0. (C) Survey spectra of particles obtained in optimised conditions (W<sub>0</sub>=25, pH=11.5) containing encapsulated rose Bengal (*i.e.*, RB@NP).

### 2.3. Luminescence characterisation

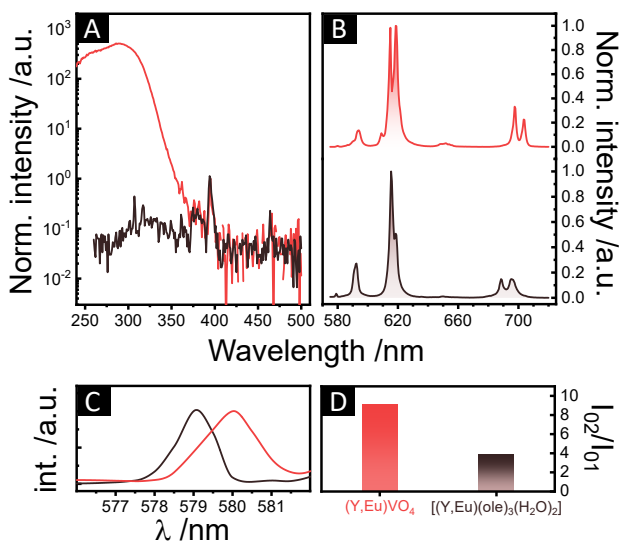


**Figure S11.** Room temperature (25 °C) luminescence spectra of the [(Y,Eu)(ole)<sub>3</sub>(H<sub>2</sub>O)<sub>2</sub>] precursor (grey line) and of the non-modified (Y,Eu)VO<sub>4</sub> particles (light red line) as powders. (A) Excitation spectra monitoring the <sup>5</sup>D<sub>0</sub>→<sup>7</sup>F<sub>2</sub> emission at λ<sub>em</sub>=619 nm. The two spectra were normalized with respect to the <sup>5</sup>L<sub>6</sub>←<sup>7</sup>F<sub>0</sub> absorption at 394 nm. (B) Emission spectra of the precursor complex (bottom, λ<sub>exc</sub>=394 nm) and of the final particles (top, λ<sub>exc</sub>=288 nm). The emission spectra were normalized with respect to the maxima. (C) Amplification of the 577-582 nm range of the emission spectra in (B) showing the <sup>5</sup>D<sub>0</sub>→<sup>7</sup>F<sub>0</sub> transitions of the [(Y,Eu)(ole)<sub>3</sub>(H<sub>2</sub>O)<sub>2</sub>] complex and the (Y,Eu)VO<sub>4</sub> particles. The spectra in (C) were normalized with respect to the maximum of the <sup>5</sup>D<sub>0</sub>→<sup>7</sup>F<sub>0</sub>. (D) Comparison of integrated intensity ratios between the <sup>5</sup>D<sub>0</sub>→<sup>7</sup>F<sub>2</sub> and <sup>5</sup>D<sub>0</sub>→<sup>7</sup>F<sub>1</sub> transitions (I<sub>02</sub>/I<sub>01</sub>) calculated from (B) for (Y,Eu)VO<sub>4</sub> and [(Y,Eu)(ole)<sub>3</sub>(H<sub>2</sub>O)<sub>2</sub>]. The <sup>5</sup>D<sub>0</sub>→<sup>7</sup>F<sub>0</sub> transition in (C) is not expected for Eu<sup>3+</sup> occupying the D<sub>2d</sub> sites in YVO<sub>4</sub>, but its occurrence is due to the low particle sizes and the presence of high amounts of surface groups causing distortions on the coordination microsymmetry<sup>7</sup>. The energy shift from 17268 cm<sup>-1</sup> for [(Y,Eu)(ole)<sub>3</sub>(H<sub>2</sub>O)<sub>2</sub>], to 17241 cm<sup>-1</sup> for (Y,Eu)VO<sub>4</sub> in (C) is due to the alterations on the coordination number and on the degree of covalence (*i.e.*, nephelauxetic effect)<sup>8</sup>.

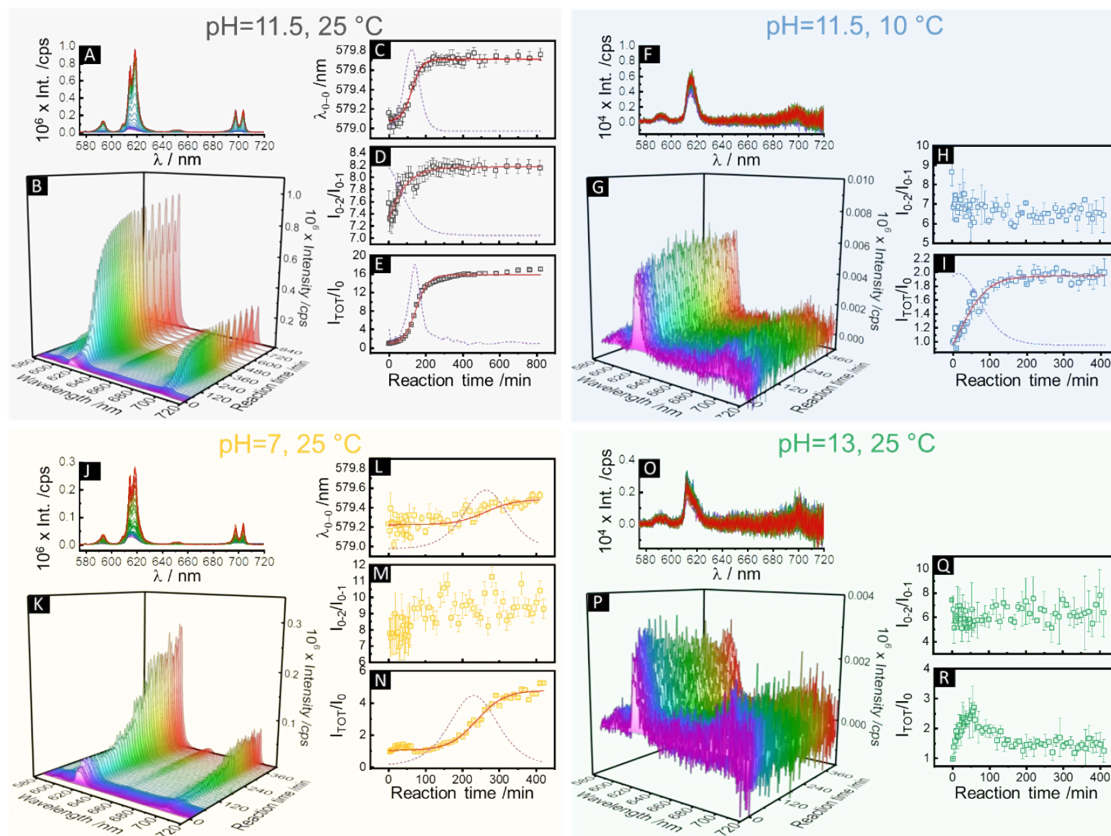


**Figure S12.** *In situ* luminescence monitoring of the formation of (Y,Eu)VO<sub>4</sub> particles in water-in-*n*-dodecane reverse microemulsions ( $W_O=25$ ) in different temperatures and pHs of the aqueous phase: (A-E) 25 °C, pH=11.5; (F-I) 10 °C, pH=11.5; (J-N) 25 °C, pH=7; (O-R) 25 °C, pH=13. The emission spectra ( $\lambda_{exc}=288$  nm) were acquired at different reaction times (violet:  $t=0$ ; red:  $t=840$  or 420 min) and are shown as (A),(F),(J),(O) superposed lines and (B),(G),(K),(P) *wavelength vs. time vs. intensity* profiles. The emission spectra enabled to measure the time evolution of different spectral parameters, namely (C),(L) the position of the  $^5D_0 \rightarrow ^7F_0$  barycenter ( $\lambda_{0-0}$ ), (D),(H),(M),(Q) the intensity ratio between the  $^5D_0 \rightarrow ^7F_2$  and  $^5D_0 \rightarrow ^7F_1$  transitions ( $I_{02}/I_{01}$ ), and (E),(I),(N),(R) the total integrated intensity normalized with respect to the integrated intensity at  $t=0$  ( $I_{TOT}/I_0$ ). The red solid lines and the dotted violet lines correspond to sigmoidal fits of the experimental data and the respective first derivatives. The  $^5D_0 \rightarrow ^7F_0$  transition is indistinguishable from the noise for (F-I) 10 °C, pH=11.5 and (O-R) 25 °C, pH=13, so  $\lambda_{0-0}$  was not determined in these cases. In (C) and (L),  $\lambda_{0-0}$  and error bars were determined by Lorentzian fits of the  $^5D_0 \rightarrow ^7F_0$  signal. Error bars for  $I_{02}/I_{01}$  and  $I_{TOT}/I_0$  were calculated from fractional uncertainties considering signal-to-noise ratios.

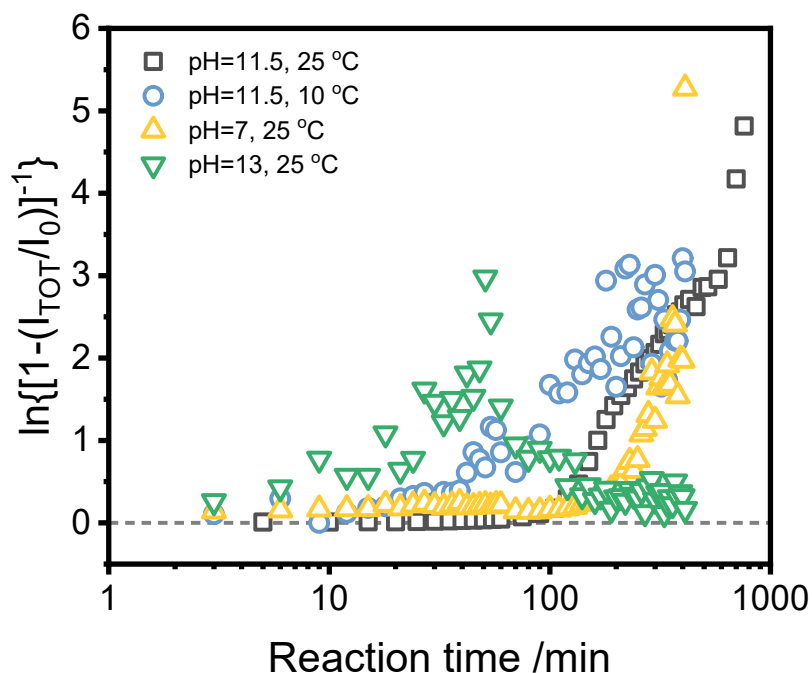


**Figure S13.** Bi-logarithmic plots of normalised total luminescence intensities ( $I_{TOT}/I_0$ ) against the reaction time for the synthesis of (Y,Eu)VO<sub>4</sub> particles ( $\lambda_{exc}=288$  nm) in reverse microemulsions ( $W_O=25$ ) at different conditions, namely pH 11.5 at 25 °C (grey squares), pH 11.5 at 10 °C (blue circles), pH 7 at 25 °C (yellow triangles), and pH 13 at 25 °C (green inverted triangles). The  $I_{TOT}/I_0$  values were obtained from data in Fig. S11. The y axis was plotted as the natural logarithm of the reciprocal of  $(1-I_{TOT}/I_0)$  to highlight induction times before burst nucleation and growth of nanoparticles.

## 2.4. Upconversion luminescence

Although photon upconversion in high phonon energy ( $>600\text{ cm}^{-1}$ ) lattices is often limited to highly crystalline particles,<sup>9</sup> nanoporous  $(\text{Y}_{0.78}\text{Yb}_{0.20}\text{Er}_{0.02})\text{VO}_4$  clearly exhibited the characteristic green  $\text{Er}^{3+}$  emissions ( ${}^2\text{H}_{11/2} \rightarrow {}^4\text{I}_{15/2}$ , 525 nm;  ${}^4\text{S}_{3/2} \rightarrow {}^4\text{I}_{15/2}$ , 545 nm) under  $\lambda_{\text{exc}} = 980\text{ nm}$  (Fig. S14), with low contribution of emissions of the  ${}^4\text{F}_{9/2}$  state in the red. The  $\text{Er}^{3+}$ -doped particles changed their emission profile after dispersion in water (Fig. S14B), with a reduced contribution of the upper  ${}^2\text{H}_{11/2}$  state in comparison to the  ${}^4\text{S}_{3/2}$  state. This is possibly due to a laser-induced local self-heating of the particles, which is further confirmed by the linear dependence of the emission intensity ratio of the thermally coupled  ${}^2\text{H}_{11/2}$  and  ${}^4\text{S}_{3/2}$  states with the pump power (Fig. S14E).<sup>10</sup> The bi-logarithmic upconversion power dependence of the  $\text{Yb}^{3+}/\text{Er}^{3+}$  couple showed negative deviations from the expected 2-photon slope ( ${}^2\text{H}_{11/2}$ :  $1.67 \pm 0.03$ ;  ${}^4\text{S}_{3/2}$ :  $1.34 \pm 0.03$ , Fig. S13C and D), due to the high Yb/Er ratio<sup>11</sup> and to competitive thermal population of  ${}^2\text{H}_{11/2}$  and non-radiative relaxation of  ${}^4\text{S}_{3/2}$ .<sup>10</sup>

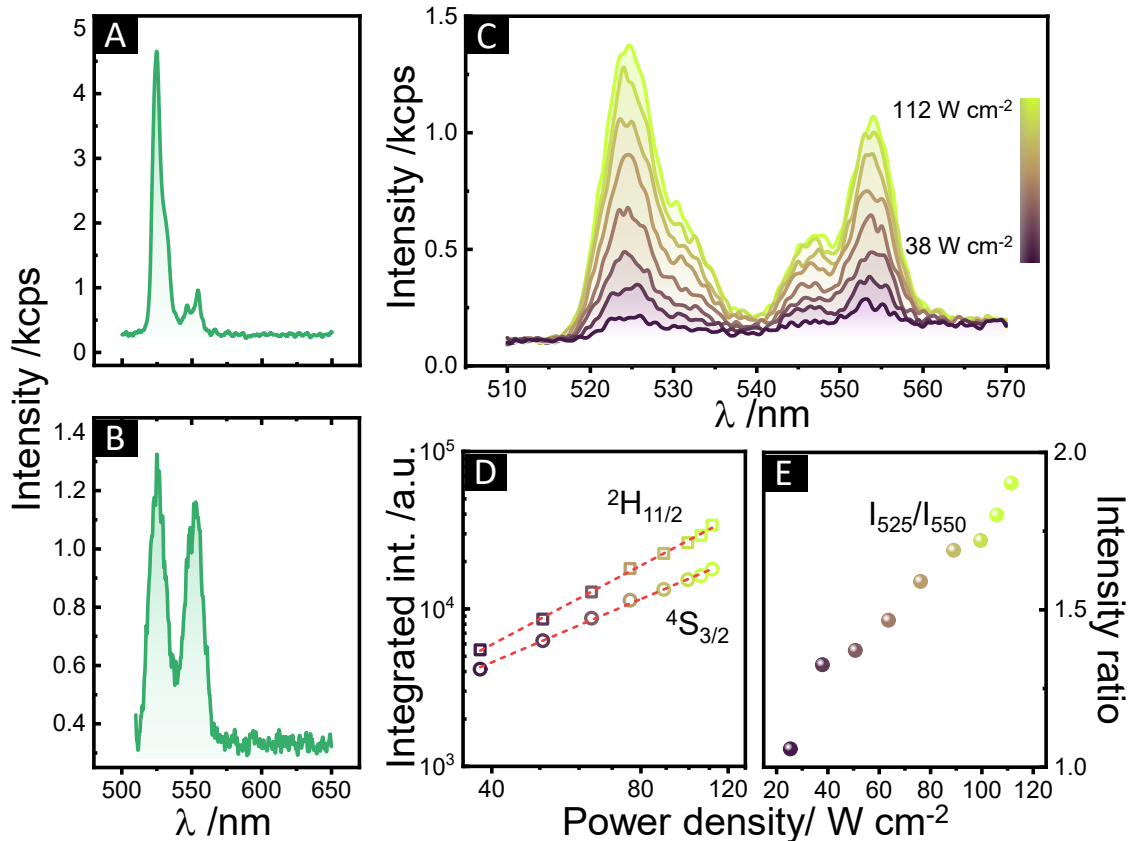


**Figure S14.** Upconversion spectra ( $\lambda_{\text{exc}}=980$  nm) of (Y,Yb,Er)VO<sub>4</sub> particles as (A) powder (90 W cm<sup>-2</sup>) (B) aqueous colloid (1 mg mL<sup>-1</sup>, 130 W cm<sup>-2</sup>). (C) Power dependence of the upconversion emission spectra of powder (Y,Yb,Er)VO<sub>4</sub> particles. (D) Dependence of the integrated intensities of the <sup>2</sup>H<sub>11/2</sub>→<sup>4</sup>I<sub>15/2</sub> (squares, slope=1.67,  $r^2=0.998$ ) and <sup>4</sup>S<sub>3/2</sub>→<sup>4</sup>I<sub>15/2</sub> (circles, slope=1.34,  $r^2=0.997$ ) against the laser power. (E) Variation of the intensity ratio between <sup>2</sup>H<sub>11/2</sub>→<sup>4</sup>I<sub>15/2</sub> and <sup>4</sup>S<sub>3/2</sub>→<sup>4</sup>I<sub>15/2</sub> Er<sup>3+</sup> transitions with the excitation power.

## 2.5. Dye encapsulation in (Y,Eu)VO<sub>4</sub> particles

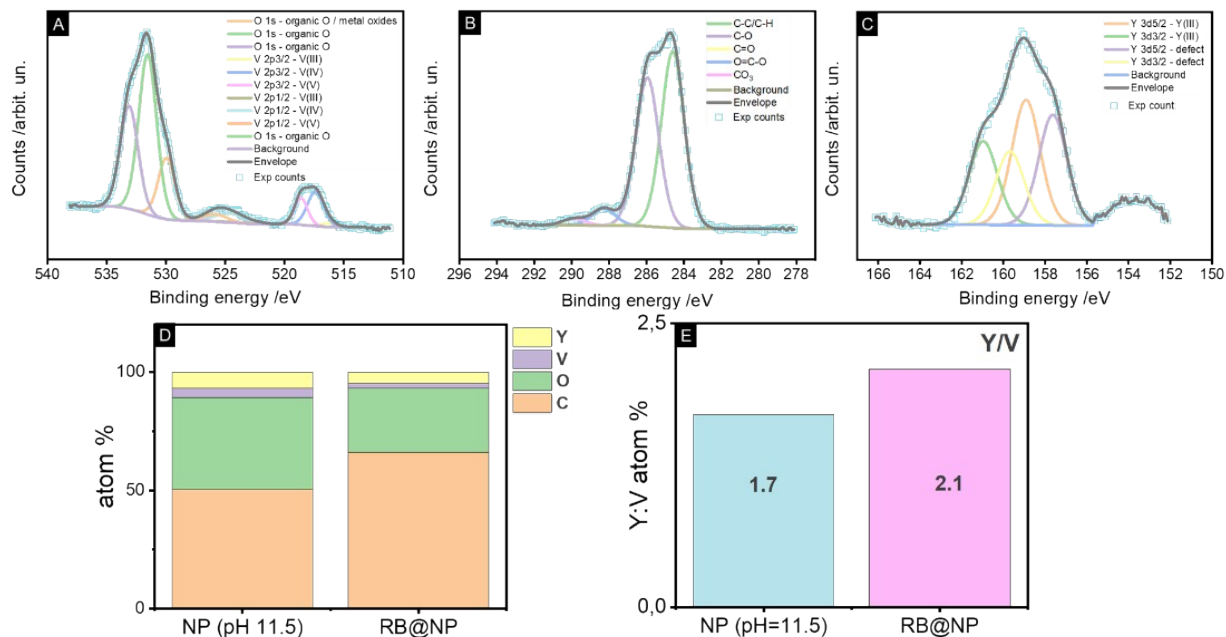


**Figure S15.** (A-C) XPS spectra of the RB@NP system (NP=(Y,Eu)VO<sub>4</sub>) obtained by reverse microemulsion synthesis ( $W_o=25$ , pH=11.5) showing the (A) O1s and V2p, (B) C1s, and (C) Y3d peaks. Survey spectra are shown in Fig. S9. (D) Compositional results (% mol) obtained from XPS spectra (Eu and residual Si are not shown for clarity). (E) Atomic ratio (mol/mol) between yttrium and vanadium.

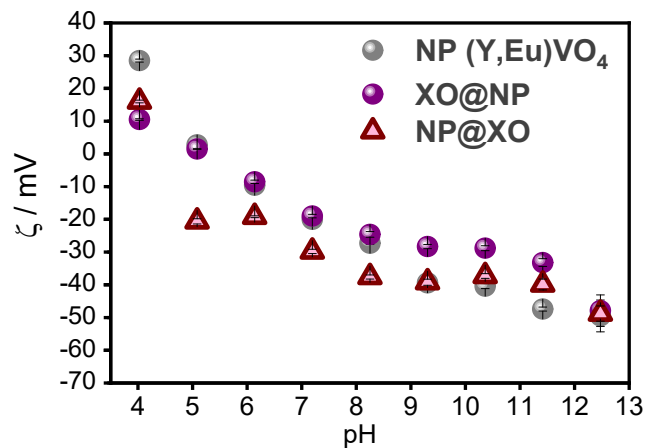


**Figure S16.**  $\zeta$  potential vs. pH curves for (Y,Eu)VO<sub>4</sub> nanoparticles prepared at  $W_O=25$  and pH=7: non-functionalised NPs (grey spheres), NPs containing encapsulated xylenol orange (XO@NP, purple spheres), and NPs contained xylenol orange at the external surface (NP@XO, wine triangles).

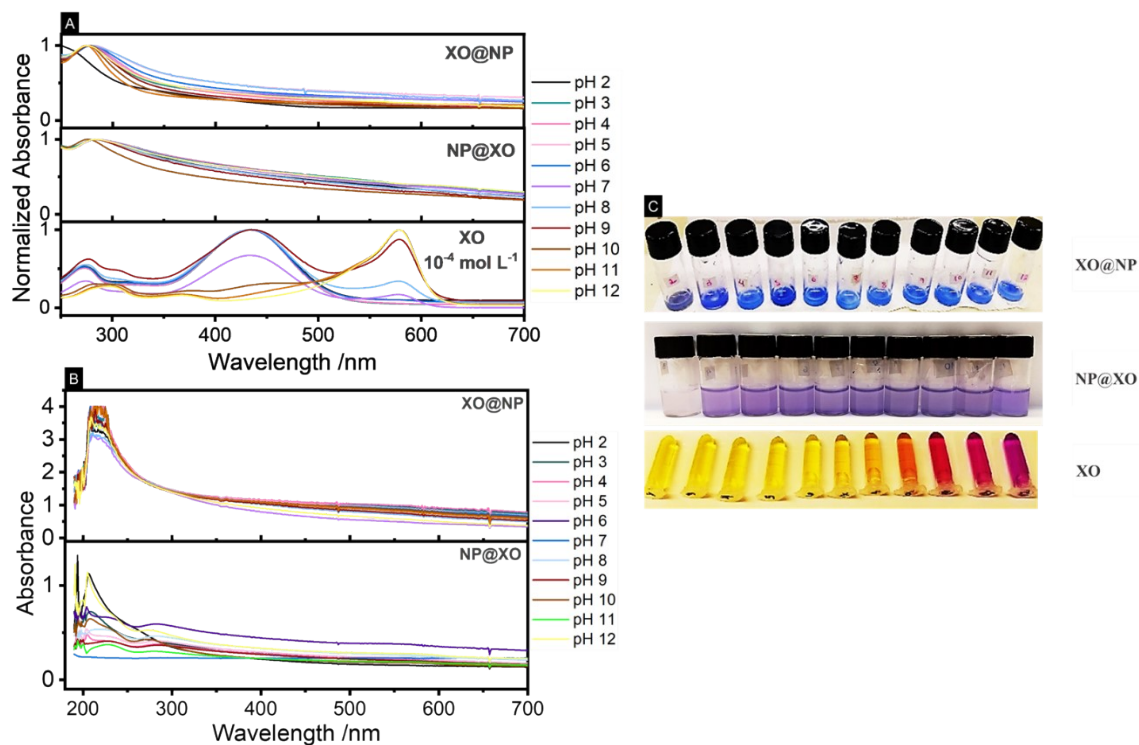


**Figure S17.** (A) UV-Vis extinction spectra of xylene orange-functionalised (Y,Eu)VO<sub>4</sub> nanoparticle suspensions (*i.e.*, XO@NP, NP@XO) in comparison to the absorption of XO solutions ( $10^{-4} \text{ mol L}^{-1}$ ) at different pH values. (B) UV-Vis extinction spectra of the XO@NP and NP@XO systems after standing for 30 days at different pH values. (C) Photographs of XO functionalised-nanoparticles in suspension (XO@NP, top; NP@XO, middle) in comparison to XO solutions (bottom) with pH ranging between 2 and 12.

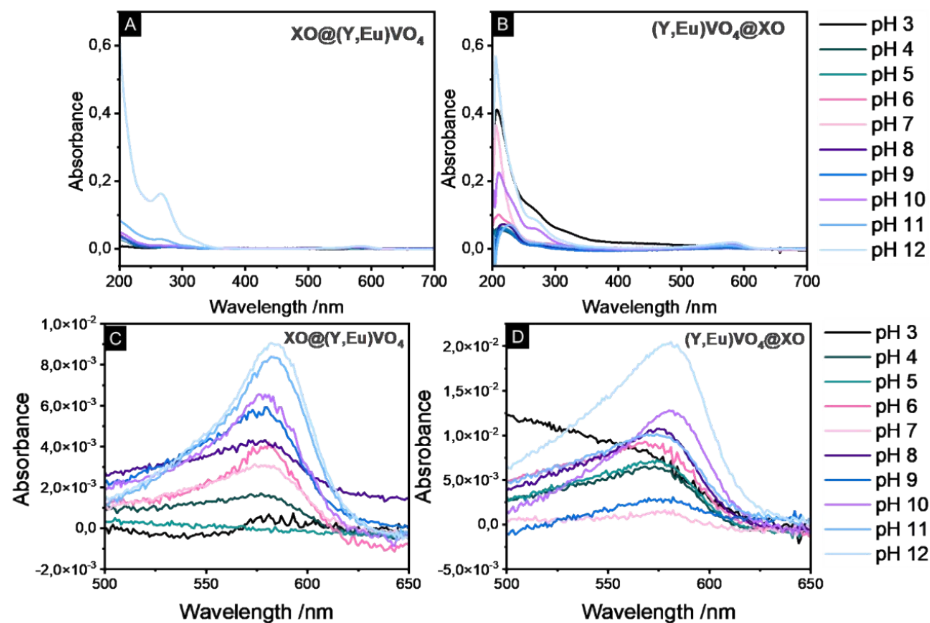


**Figure S18.** UV-Vis absorption spectra of supernatants obtained after exposing (A)  $XO@NP$  and (B)  $NP@XO$  systems to different pHs ranging between 3 and 12 for 30 days. (C) and (D) show the 500-650 nm range of (A) and (B), respectively, highlighting the xylene orange absorption.

### 3. REFERENCES

1. B. R. Anderson, R. Gunawidjaja and H. Eilers, *J. Lumin.*, 2018, **204**, 341–348.
2. B.L. Gupta, *Talanta*, 1974, **6**, 683-684.
3. (a) J. Ilvasky and P.R. Jemain, *J. Appl. Cryst.*, 2009, **42**, 347-353. (b) A. Guinier and G. Fournet, *Small-Angle Scattering of X-Rays*, John Wiley and Sons, New York (1955).
4. G. Beaucage, *J. Appl. Crystallogr.*, 1995, **28**, 717-728.
5. (a) J.N. Israelachvili and R.M. Pashley, *J. Coll. Int. Sci.*, 1984, **98**, 500-514. (b) R.M. Pashley, P.M. McGuiggan, R.G. Horn, B.W. Ninham, *J. Coll. Int. Sci.*, 1988, **126**, 569-578.
6. U. Holzwarth, N. Gibson, *Nat. Nanotechnol.*, 2016, **6**, 534.
7. K. Binnemans, *Coord. Chem. Rev.*, 2015, **295**, 1–45.
8. P.A. Tanner, Y.Y. Yeung, L. Ning, *J. Phys. Chem. A*, 2013, **117**, 2771–2781.
9. A. Nadort, J. Zhao and E. M. Goldys, *Nanoscale*, 2016, **8**, 13099- 13130.
10. A. H. Li, Z. J. Sun and Q. Lü, *J. Nanoparticle Res.*, 2013, **15**, 1-10.
11. V. T. Vera, D. M. Gonzalez, D. J. R. Ramos, A. Igalla, M. Laurenti, R. C. Caceres, E. L. Cabarcos, E. Díaz and J. R. Retama, *J. Mater. Chem. C*, 2021, **9**, 8902-8911.